Generation of multiple plasmons in strontium niobates mediated by local field effects

Tao Zhu,[1,2] Paolo E. Trevisanutto,[1,2,3] Teguh Citra Asmara,[2,4] Lei Xu,[1] Yuan Ping Feng,[1,3] and Andrivo Rusydi[1,2,3,4,5,*]

[1]*Department of Physics, National University of Singapore, Singapore 117542, Singapore*
[2]*Singapore Synchrotron Light Source, National University of Singapore, Singapore 117603, Singapore*
[3]*Center for Advanced 2D Materials, National University of Singapore, Singapore 117542, Singapore*
[4]*NUSNNI-NanoCore, National University of Singapore, Singapore 117411, Singapore*
[5]*NUS Graduate School for Integrative Sciences and Engineering, National University of Singapore, Singapore 117456, Singapore*

Recently, an anomalous generation of multiple plasmons with large spectral weight transfer in the visible to ultraviolet range (energies below the band gap) has been experimentally observed in the insulatinglike phase of oxygen-rich strontium niobium oxides ($SrNbO_{3+\delta}$). Here, we investigate the ground-state and dielectric properties of $SrNbO_{3+\delta}$ as a function of δ by means of extensive first-principle calculations. We find that in the random phase approximation by taking into account local field effects, our calculations are able to reproduce both the unconventional multiple generations of plasmons and the spectral weight transfers, consistent with experimental data. Interestingly, these unconventional plasmons can be tuned by oxygen stoichiometry as well as microscopic superstructure. This unusual predominance of local field effects in this class of materials is ascribed to the strong electronic inhomogeneity and high polarizability and paves a new path to induce multiple plasmons in the untapped visible to ultraviolet ranges of insulatinglike oxides.

I. INTRODUCTION

The $Sr_{1-x}Nb_{1-y}O_{3+\delta}$ oxides have been known for their rich properties, which strongly depend on their oxygen stoichiometry [1–9]. Upon increasing their oxygen content, the oxides can be transformed from the three-dimensional metal, $SrNbO_3$, to the quasi-one-dimensional metal, $SrNbO_{3.4}$, and, finally, to the ferroelectric insulator, $SrNbO_{3.5}$. Recently, these oxides have been reported to exhibit several exotic phenomena based on their anomalous plasmon behaviors. The metallic perovskite $SrNbO_3$, for instance, has been found to be a potentially good visible-light photocatalyst for water splitting applications [10], and this photoactivity has been reported to be driven by plasmon-based resonances [11] instead of the more usual interband excitations. More interestingly, under oxygen enrichment, $SrNbO_{3+\delta}$ has been reported to exhibit an anomalous multiple bulk plasmon generation [12].

These plasmons have shown several unconventional features [12]. They have been detected, intriguingly, in insulatinglike samples with room-temperature resistivity up to 6 Ω cm. As a function of δ, they became weaker and eventually merged into a single plasmon in samples with a higher conductivity. Moreover, due to its high resistivity, the real part of the complex dielectric function, ε_1, has no negative value below the plasmon energies. These indicate that these plasmons are different from the conventional bulk plasmons, as the latter typically shows a 0 cross of the real dielectric function. Finally, the losses of these plasmons are fairly low, i.e., several times lower than that in gold, which provides a

new direction for plasmonic research in the visible-ultraviolet ranges.

The origin of these unconventional plasmons remains an open question and a proper theoretical description is still lacking. Previously, Asmara *et al.* [12] suggested a possible explanation using a phenomenological semiclassical model with adjustable parameters. On the other hand, calculations based on a dynamical mean-field theory framework [13,14] have shown that in strongly correlated systems, qualitatively to some extent, similar spectral weight transfers and generation of multiple anomalous plasmons can occur [15]. However, these theoretical results were not wholly consistent with the experimental findings [12], in particular, regarding both the predicted energy ratio of the plasmon peak energies and the potential effect of oxygen doping on the formation of plasmons. More importantly, the previously calculated absorption spectra were obtained by neglecting the microscopic fluctuations that may give rise to local field effects (LFEs) [16–22]. This was despite the importance of LFEs in modifying the shape and intensity of loss function spectra in various materials, particularly at high energies where semicore-localized electrons are involved [23].

In this article, we present a systematic study of the mechanisms and properties of plasmons in strontium niobates using *ab initio* calculations. Within the linear-response time-dependent density functional theory (DFT) framework [24], we have calculated the complex dielectric and the loss functions of $SrNbO_{3+\delta}$ as a function of the oxygen doping and its microscopic superstructures. In the random phase approximation (RPA) [25] and taking into account LFEs, we show that the fundamental properties of this multiple plasmon formation and their evolution are well described and in good agreement with experimental findings [12]. For $SrNbO_3$, the
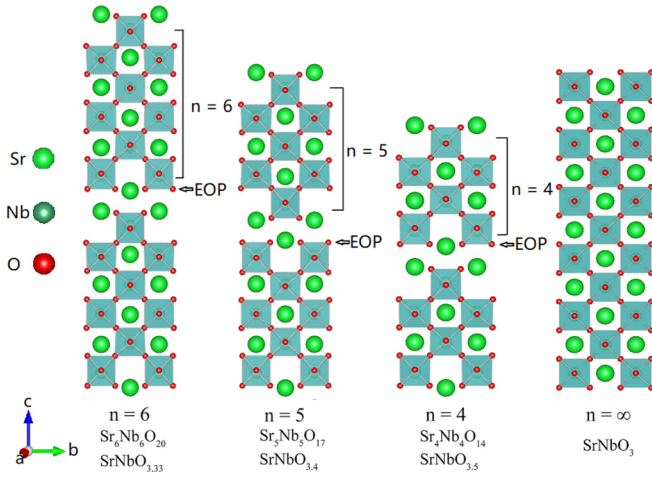
*phyandri@nus.edu.sg

FIG. 1. Sketch of crystal structures of the perovskite-related layered series $Sr_nNb_nO_{3n+2}$ for $n = 6$, 5, 4, and ∞. Extra oxygen planes (EOPs) are shown between two neighboring layers.

experimental plasmon is reproduced and this is described as an interplay of interband and intraband transitions. LFEs do not play any role. In contrast, for oxygen-rich $SrNbO_{3+\delta}$, an LFE enhancement yields drastic spectral weight transfers and multiple unconventional plasmons arise. Our analysis shows that the LFEs stem from the localization of Nb $4d$ electrons in cooperation with the high polarizability of the oxygen-rich $SrNbO_{3+\delta}$ systems.

The article is divided into five sections. In Sec. II, we introduce the theoretical methods and parameters used in the first-principle calculations. The structure of two typical $SrNbO_{3+\delta}$'s and the DFT-based RPA method with the inclusion of LFEs are discussed. The calculated results for the electronic structure and dielectric properties of $SrNbO_3$ and two configurations of $SrNbO_{3.4}$ are reported in Sec. III. In Sec. IV, we propose a theoretical explanation for the experimental detection of these multiple plasmons and we analyze the importance of the extra oxygen plane (EOP) in determining the creation of these unconventional multiple plasmons. The last section (Sec. V) summarizes and concludes the main achievements of this work.

II. METHODS

As representative cases, we study the effects of LFEs on $SrNbO_{3+\delta}$ as a function of the oxygen doping, i.e., $SrNbO_3$ and $SrNbO_{3.4}$, and microscopic superstructure of alternating layers from $SrNbO_{3.33}$ and $SrNbO_{3.5}$. Their complex dielectric functions, $\varepsilon = \varepsilon_1 + i\varepsilon_2$, and loss functions, $-Im[\varepsilon^{-1}]$, are calculated with and without LFEs and then compared with experimental data [12]. In terms of structure, the ideal structure of $SrNbO_3$ is created by a three-dimensional network of corner-sharing NbO_6 octahedra with Sr atoms filling in the center of the network. With oxygen enrichment, however, the structure of $SrNbO_{3.4}$ becomes homologous to that of the layered perovskite series of the $Sr_nNb_nO_{3n+2}$ family as shown in Fig. 1. These series can be derived from the three-dimensional network of the $SrNbO_3$ perovskite structure by separating the NbO_6 octahedra with EOPs parallel to the [101] perovskite

planes every n unit cells, creating a layered structure with stacks of slabs along their c axes [6]. This makes the structure of $SrNbO_{3.4}$ strongly anisotropic, which creates strong charge inhomogeneity and high polarizability along one particular crystal orientation [7,8].

We began with DFT calculations of the ground-state property of $SrNbO_{3+\delta}$ using the Vienna *ab initio* simulation package (VASP) [26,27]. The projector-augmented wave (PAW) method [28] and the Perdew-Burke-Ernzerhof (PBE) exchange-correlation functional within the GGA [29] were employed. A plane-wave basis set with a 500-eV energy cutoff was used to expand the Kohn-Sham [30] wave functions. The Sr $4s4p5s$, Nb $4p5s4d$, and O $2s2p$ orbitals were treated as valence states. The irreducible Brillouin zone of cubic $SrNbO_3$ was sampled by a $13 \times 13 \times 13$ Γ centered Monkhorst-Pack [31] grid, and a $9 \times 7 \times 1$ Γ centered Monkhorst-Pack grid was employed for the supercell of layered $SrNbO_{3+\delta}$. The Gaussian smearing with a width of 0.05 eV was adopted to treat the partial occupancies. The lattice constant of the fully relaxed structure of $SrNbO_3$ is $a = b = c = 4.07$ Å and the optimized lattice parameter of the supercell of $SrNbO_{3.4}$ is $a = 4.03$ Å, $b = 5.75$ Å, and $c = 33.45$ Å. These values are in good agreement with those reported in previous studies [8,9].

The dielectric matrix is calculated on top of the ground-state calculations. We further follow with a simple RPA approach in which the Fourier transform of the symmetric microscopic dielectric matrix is given by

$$\varepsilon_{\mathbf{G},\mathbf{G}'}(\mathbf{q}, \omega) = \delta_{\mathbf{G},\mathbf{G}'} - v(\mathbf{q} + \mathbf{G})\chi^0_{\mathbf{G},\mathbf{G}'}(\mathbf{q}, \omega), \quad (1)$$

where $\mathbf{G}$ and $\mathbf{G}'$ are reciprocal lattice vectors, $\mathbf{q}$ is the Bloch vector in the first Brillouin zone, and v is the bare Coulomb interaction. The independent-particle irreducible polarizability matrix, $\chi^0_{\mathbf{G},\mathbf{G}'}(\mathbf{q}, \omega)$, is summed over transitions between occupied and empty states and can be constructed from Kohn-Sham wave functions ψ and eigenvalues ϵ [24,32].

The macroscopic dielectric function (which is comparable to experiment) is determined at the limit of $\mathbf{q} \to 0$ as

$$\varepsilon_M(\omega) = \lim_{\mathbf{q} \to 0} \frac{1}{\varepsilon^{-1}_{\mathbf{G}=0,\mathbf{G}'=0}(\mathbf{q}, \omega)}. \quad (2)$$

The energy loss functions are then given by $-Im[\varepsilon_M^{-1}]$ for a vanishingly small wave vector [32].

The off-diagonal elements of the dielectric function in the matrix inversion of Eq. (2), $\varepsilon^{-1}_{\mathbf{G},\mathbf{G}'}(\mathbf{q}, \omega)$, are responsible for the LFEs and they become important in inhomogeneous systems where localization of atomic orbitals plays a major role (as in d and f transition metals). Alternatively, the LFEs can be included in ε_M explicitly by constructing a modified response function [32],

$$\varepsilon_M(\omega) = 1 - \lim_{\mathbf{q} \to 0} v_0(\mathbf{q})\bar{\chi}_{\mathbf{G}=0,\mathbf{G}'=0}(\mathbf{q}, \omega), \quad (3)$$

where we have introduced $\bar{\chi}$, which satisfies the Dyson-like equation $\bar{\chi} = \chi^0 + \chi^0\bar{v}\bar{\chi}$, and $\bar{v}$ is the bare Coulomb interaction (excluding the long-range term in v). In the Dyson-like equation for $\bar{\chi}$, the second term with $\bar{v}$ plays the role of LFEs [32,33]. Neglecting this term in the expression of $\bar{\chi}$ yields the so-called independent-particle random phase approximation
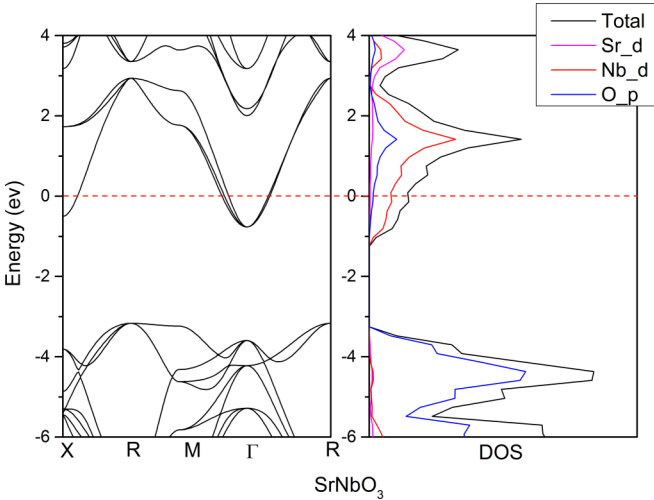
FIG. 2. Band structure and density of states of $SrNbO_3$. The dashed red line represents the Fermi level.

FIG. 3. Calculated macroscopic complex dielectric and loss functions of $SrNbO_3$. The calculated (a) real part, ε_1, and (b) imaginary part, ε_2, of the complex dielectric function as well as (c) the loss function, $-\mathrm{Im}[\varepsilon^{-1}]$, of $SrNbO_3$ are compared with those from experiments (Exp) [12]. RPA and IP-RPA refer to calculation with and without LFEs, respectively (they almost overlapped). RPA + Intra refers to the RPA calculation which includes intraband transitions. The dashed horizontal line indicates the 0 of ε_1, to pinpoint the conventional plasmon peak energy.

(IP-RPA),

$$\varepsilon_M(\omega) = 1 - \lim_{\mathbf{q}\to 0} v_0(\mathbf{q})\chi^0_{\mathbf{G}=0,\mathbf{G}'=0}(\mathbf{q}, \omega)$$
$$= \lim_{\mathbf{q}\to 0} \varepsilon_{\mathbf{G}=0,\mathbf{G}'=0}(\mathbf{q}, \omega), \qquad (4)$$

where the off-diagonal elements in the matrix inversion of Eq. (2) are neglected. In addition, we have also included the intraband transitions in the RPA polarizability by using the DP code [34] to quantify the effects of the Drude tail.

III. RESULTS

A. SrNbO$_3$

The calculated band structure and DOS of $SrNbO_3$ are shown in Fig. 2. The $SrNbO_3$ is a metallic material, as the Fermi energy (E_F) crosses the conduction band. The Nb $4d$ orbitals, which split into the triply degenerated t_{2g} and the doubly degenerated e_g in the octahedral field, are responsible for its metallicity. Thus, little distortion of the NbO_6 octahedra in $SrNbO_3$ has been reported [9]. Interestingly, an apparent large indirect band gap (~2.3 eV) can be seen just below the E_F. The conduction-band minimum lies at the Γ point, and the valence-band maximum at the R point. The existence of this large band gap below the E_F suggests that the photocatalytic activity of $SrNbO_3$ may arise from hot electrons generated from the decay of the plasmon resonance instead of interband transitions [11]. From the site-projected DOS, it can be seen that the oxygen p orbital contributed most of the DOS just below the Fermi energy and chemical bonding exists between electrons from O $2p$ orbitals and Nb $4d$ orbitals.

Figure 3 shows the calculated complex dielectric and loss functions of $SrNbO_3$ compared with experimental data from the $Sr_{1-x}NbO_{3+\delta}$ film deposited under a low oxygen pressure (labeled lp-SNO in Ref. [12]). As shown, in the experimental results, metallic $SrNbO_3$ has a conventional single-plasmon resonance at ~1.9 eV, which coincides with the 0 of ε_1. This apparent plasmon peak, located at ~1.9 eV, has an energy similar to that of the absorption edge in the photocatalysis experiment, which implies its plasmonic origin [11].
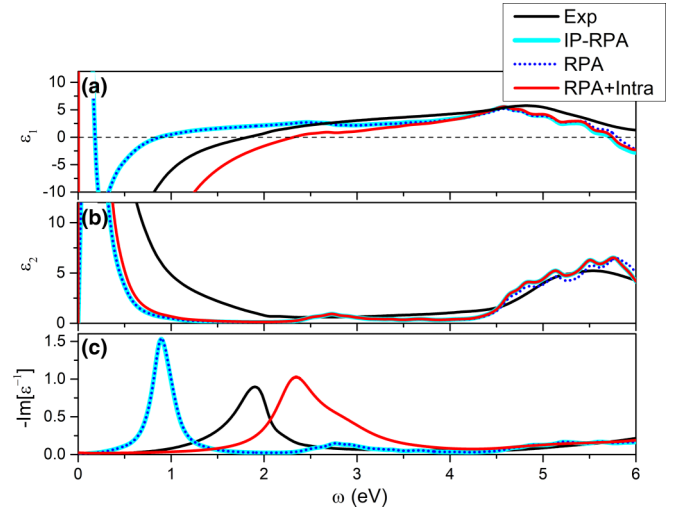
The IP-RPA calculations are sufficient to reproduce this main feature. Since the IP-RPA calculations regard the electrons as independent, noninteracting particles, this indicates that the partially filled $4d$ orbitals do not induce strong correlations in $SrNbO_3$, making it a weakly correlated material. The inclusion of LFEs also does not change the calculated spectra, indicating that LFEs do not play a role here and $SrNbO_3$ is electrically homogeneous. The underestimation of the conventional plasmon resonance energy in the IP-RPA calculation can be corrected by adding intraband transitions of Nb $4d$ orbitals, in addition to the interband transitions from O $2p$ to Nb $4d$. Thus, the plasmon at ~1.9 eV in $SrNbO_3$ originates from the cumulative effects of interband and intraband transitions.

B. SrNbO$_{3.4}$ ($n = 5$)

Because the experimental sample shows a layered structure in which every few NbO_6 octahedra are separated by EOPs., we calculated the dielectric function and loss function of $SrNbO_{3.4}$ along the c axis as shown in Fig. 5. We can see that the situation for $SrNbO_{3.4}$, on the other hand, is totally different. Because $SrNbO_{3.4}$ is nominally not fully oxidized, the IP-RPA again predicts the existence of a metallic conventional plasmon peak. However, the experimental data have shown that the Drude tail was absent in the ε_2 spectrum and the ε_1 spectrum remained positive in all energy ranges, indicating that it has an insulatinglike behavior. Furthermore, unlike for $SrNbO_3$, the conventional single plasmon peak is not present; instead, unconventional multiple plasmon peaks have emerged at ~1.7, ~3.0, and ~4.0 eV accompanied by spectral weight transfers.
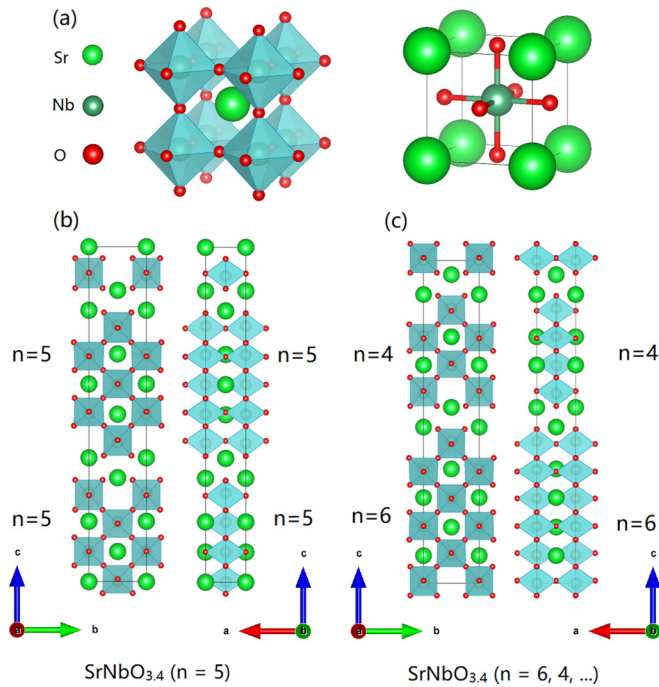
FIG. 4. Crystal structure of $SrNbO_3$ and two configurations of $SrNbO_{3.4}$. (a) $SrNbO_3$, (b) $SrNbO_{3.4}$ ($n = 5$), and (c) $SrNbO_{3.4}$ ($n = 6, 4, \ldots$) projected along the a and b axes. In each layer, the connection of NbO_6 octahedra behaves zigzaglike along the b axis and chainlike along the a axis. Every nearest-neighbor layer has a height difference of a half of the NbO_6 octahedron body diagonal along the a axis, while every next-nearest-neighbor layer has the same height.

These fundamental differences between $SrNbO_{3.4}$ and $SrNbO_3$ suggest that the mechanisms behind these plasmons are very different from those of conventional plasmons in metals. It has been shown in the previous theoretical study [15] that vertex corrections might indeed induce spectral weight transfers and create multiple plasmon peaks in strongly correlated systems. However, as shown in Fig. 3, the partially filled Nb $4d$ orbitals do not induce strong electron correlations in $SrNbO_3$. More importantly, the predicted energy and ratio of plasmon peaks are different from those of the observed unconventional plasmons in $SrNbO_{3.4}$ [12], suggesting that other mechanisms should be involved. On the other hand, it has been shown recently that in the absorption spectrum of correlated materials, such as VO_2, LFEs make a strong contribution to the optical spectra due to the localized nature of electron-hole pairs [35]. On the c axis, $SrNbO_{3.4}$ has a layered structure generated by the EOPs (Fig. 4), which confine the Nb $4d$ electrons within each slab and, further, create a strong electronic inhomogeneity and high polarizability along the c axis. Therefore strong modification of the spectrum by LFEs may be expected.

Our main theoretical result, as shown in Fig. 5, is that LFEs are surprisingly dominant in the $SrNbO_{3.4}$ complex dielectric and loss function spectra. When LFEs are introduced into the RPA calculations, the conventional plasmon at ~ 1.2 eV is suppressed and new unconventional multiple plasmons at ~ 1.9 and ~ 2.9 eV are generated instead. The calculated ε_1
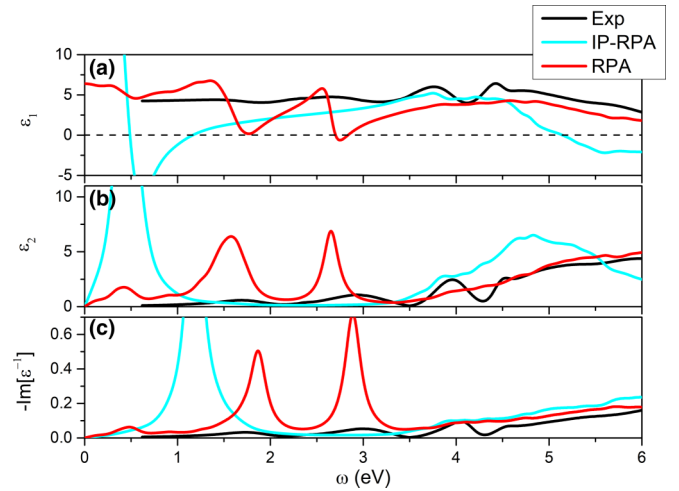

FIG. 5. Calculated macroscopic complex dielectric and loss functions of $SrNbO_{3.4}$ along the c axis. The calculated (a) real part, ε_1, and (b) imaginary part, ε_2, of the complex dielectric function as well as (c) the loss function, $-Im[\varepsilon^{-1}]$, of $SrNbO_{3.4}$ are compared with those from experiments (Exp) [12]. RPA and IP-RPA refer to the calculation with and without LFEs, respectively. The dashed horizontal line indicates the 0 of ε_1, to pinpoint the conventional plasmon peak energy.

also becomes positive in almost all energy ranges, which indicates its insulating feature. All of these are consistent with the experimental data [12].

C. $SrNbO_{3.4}$ ($n = 4, 6, \ldots$)

From Eq. (3), it can be understood that, in addition to the electrical inhomogeneity, strong LFEs can also originate from a large Kohn-Sham polarizability χ^0, for example, in strongly polarized systems with very localized orbitals [22,35]. To further investigate the effects of high polarizability and also to account for possible nonuniformities in the experimental $SrNbO_{3.4}$ sample [12], we performed calculations on an intercalated $SrNbO_{3.4}$ structure as described below. Within the layered $Sr_nNb_nO_{3n+2}$ series, $SrNbO_{3.4}$ is formed when $n = 5$, which means that adjacent EOPs are separated by a layer five NbO_6 octahedra thick along the c axis. In the intercalated structure, the stacking sequence is tweaked so that the layers are intercalated in four and six NbO_6 octahedra thicknesses instead, i.e., $n = 4, 6, 4, 6$, etc. As shown in Fig. 4, this alternate configuration can be created by combining layers from metallic $SrNbO_{3.33}$ ($n = 6$) and insulating $SrNbO_{3.5}$ ($n = 4$) compounds. While the number of oxygen atoms and total electron density remain nominally (almost) the same as for $SrNbO_{3.4}$, this alternate structure contains units of fully oxidated ($n = 4$) $SrNbO_{3.5}$, which is a ferroelectric with extraordinary high values of polarizability (at room temperature, $\varepsilon_{1a} = 75$, $\varepsilon_{1b} = 43$, $\varepsilon_{1c} = 46$) [36]. In addition, our DFT calculations show that the ground-state free energy for standard $SrNbO_{3.4}$ ($n = 5$) and intercalated $SrNbO_{3.4}$ ($n = 4, 6, \ldots$) configurations are very close (-506.36 and -506.28, respectively), implying that this new configuration is stable. Moreover, this $SrNbO_{3.4}$ configuration may also be a better representative of the
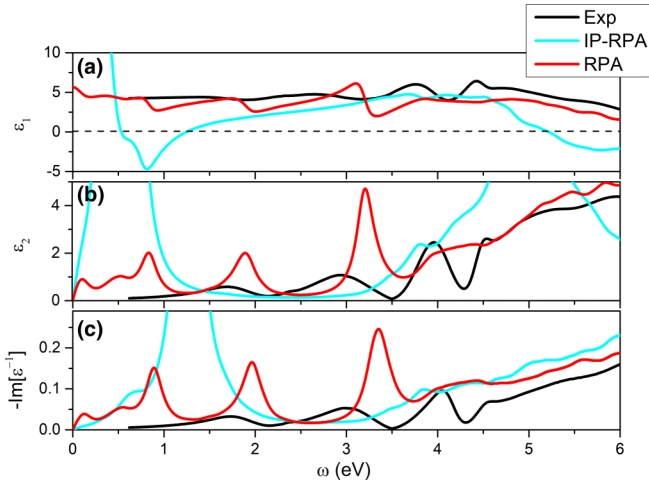
FIG. 6. Calculated macroscopic complex dielectric and loss functions of $SrNbO_{3.4}$ with an alternate structure along the c axis. The calculated (a) real part, ε_1, and (b) imaginary part, ε_2, of the complex dielectric function as well as (c) the loss function, $-Im[\varepsilon^{-1}]$, of $SrNbO_{3.4}$ with an alternate structure ($n = 4, 6, \ldots$) are compared with those from experiments (Exp) [12]. RPA and IP-RPA refer to the calculation with and without LFEs, respectively. The dashed horizontal line indicates the 0 of ε_1, to pinpoint the conventional plasmon peak energy.

experimental oxygen-rich $SrNbO_{3+\delta}$ samples, which showed some signs of similar nonuniformity in their growth [12].

As Fig. 6 shows, the IP-RPA loss function of $SrNbO_{3.4}$ ($n = 4, 6, \ldots$) is almost unchanged in comparison with that of the standard $SrNbO_{3.4}$ ($n = 5$) because they have almost the same charge density. In contrast, in the RPA + LFEs results, three main peaks appear in both the dielectric and the loss functions at almost the same energies, ~ 0.9, ~ 2.0, and ~ 3.3 eV, even more consistent with experimental data. For comparison, in the RPA + LFEs calculations using the standard ($n = 5$) structure (Fig. 3), only two prominent loss function peaks appear within the experimental measurement limit of 0.6 to 6.0 eV and these peaks are ~ 0.3 eV blue-shifted compared to the corresponding dielectric function peaks in ε_2. The absence of these peak shifts from the alternate structure implies stronger LFEs, which suppress the long-range Coulomb interaction at the response function kernel in time-dependent density functional theory [33]. This can be expected from the highly polarizable ($n = 4$) $SrNbO_{3.5}$ units embedded within. The intensities of calculated peaks are also less intense compared to the standard structure, which allows these anomalous plasmons to have low loss, consistent with experimental data. This intensity damping is attributed to the repulsive nature of LFEs (as a Coulomb interaction) between charge density waves [22]. This means that the anomalous plasmon peaks in $SrNbO_{3.4}$ do indeed arise from the LFEs.

IV. DISCUSSION

We have shown that LFEs are essential to create multiple unconventional plasmons with spectral weight transfers. The calculated peaks do appear to be globally red-shifted compared with experimental data. This could be due to the fact that
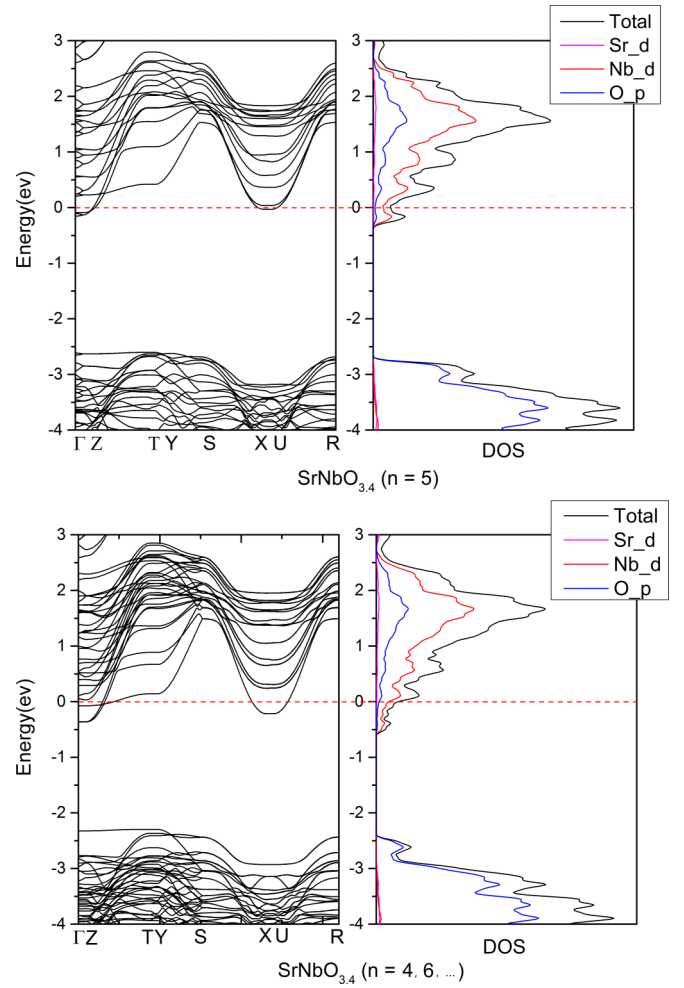

FIG. 7. Band structure and density of states of $SrNbO_{3.4}$ ($n = 5$) and $SrNbO_{3.4}$ ($n = 4, 6, \ldots$). The dashed red line represents the Fermi level.

electron-electron and electron-hole interactions are neglected in the RPA. Nevertheless, $SrNbO_{3.4}$ has a metallic behavior which suppresses these interactions. From our calculations and in comparison to experimental data, it can be clearly inferred that LFEs are the main cause of the spectral weight transfer from a single conventional plasmon peak to higher energies with the subsequent creation of multiple plasmon peaks.

The next question is related to which bands contribute to the creation of these unconventional plasmons. In Fig. 7, the DFT band structures and DOS of the two introduced types of $SrNbO_{3.4}$ are shown. Similarly to $SrNbO_3$, both configurations of $SrNbO_{3.4}$ show a metallic feature, as the E_F crosses the conduction band. For these two types of oxygen-rich materials, the E_F is placed at the bottom of the conduction band, which indicates a lower conductivity than in $SrNbO_3$. The direct band gap, ~ 2.3 eV, is found at the Γ point and it is just below the E_F in both configurations. From the IP-RPA results, the plasmon peak is placed at ~ 1.2 eV, which implies that the peaks in the loss function do not likely originate from interband transitions alone. Moreover, it should be noted that the multiple plasmon frequencies as

shown in the RPA spectra are created by a mixture of different independent transitions when the LFEs are taken into account. Thus, we infer that these multiple plasmons are still collective excitations but involving structural confinement of Nb 4d electrons where d-d transitions play a major role. On the other hand, a strong modification of the spectra from LFEs suggests a strong electronic inhomogeneity along the c axis. Previous experimental and numerical reports [7,8,12,36] show that the density of occupied states at the E_F mainly comes from the central Nb atoms located in the middle of the slabs, whereas the contributions of the other two Nb sites decrease substantially towards the edges. This could be an indication that the EOP is able to confine the free Nb 4d electrons to the center area of slabs and generate strong LFEs.

To further investigate the effects of structural confinement caused by the EOP, we consider the anisotropic structure of oxygen-rich SrNbO$_{3+\delta}$. Unlike the cubic perovskite structure of SrNbO$_3$, the structure of SrNbO$_{3.4}$ is highly anisotropic. The EOP separates different layers along the c axis, which precludes free electron transport to the neighboring layers. On the other hand, as shown in Fig. 4, within each slab the NbO$_6$ octahedra extend zigzaglike along the b axis and chainlike along the a axis. This strong structural anisotropy makes SrNbO$_{3.4}$ a low-dimensional metal [7,8]. From the band structure as shown in Fig. 7, the E_F crosses the conduction band along the Γ-Z and X-U directions. At the same time, there is no apparent band dispersion along these two directions. This indicates an insulating feature along the c axis, in agreement with the experimental result that the conductivity along the c axis is quite low [6,7].

In Fig. 8 we show the calculated dielectric and loss function of SrNbO$_{3.4}$ ($n = 5$) along different axes. It is shown that for the electric field along the a and b axes, the IP-RPA and RPA calculations give almost-identical spectra. This implies that LFEs have little impact on spectra along these directions and thus further highlights the importance of the EOP in creating strong LFEs. Interestingly, although the a axis retains the same Nb-O chainlike structure as isotropic SrNbO$_3$, the ε_1 stays positive, which indicates an insulating character. This is consistent with the previous report [7] that a unique small energy gap at the Fermi level exists in this conducting chain at low temperatures. Further analyses show that this temperature-driven metal-to-insulator transition may be created by the formation of a charge density wave below the Peierls transition [7,8]. Under IP-RPA, the b axis and the c axis have similar spectra. A conventional-type plasmon is shown on both axes at ∼1.2 eV. However, when LFEs are included, only the plasmon peak along the c axis transfers to a higher energy and splits into two branches, located at ∼1.9 and ∼2.9 eV, while the loss function along the b axis shows only a slight blue shift. This indicates that the confinement caused by the EOP is crucial in creating unconventional multiple plasmons. As an interesting comparison, a strong modification of the loss function caused by LFEs has been found in rutile TiO$_2$, where semicore Ti 3p electrons are involved [23]. However, as we have shown in Fig. 3, opposite to the SrNbO$_{3+\delta}$ case, the partially filled Nb 4d orbitals do not induce strong LFEs in SrNbO$_3$. Instead, the strong localization of Nb 4d electrons in oxygen-rich SrNbO$_{3+\delta}$ samples is induced by the EOP, which plays a
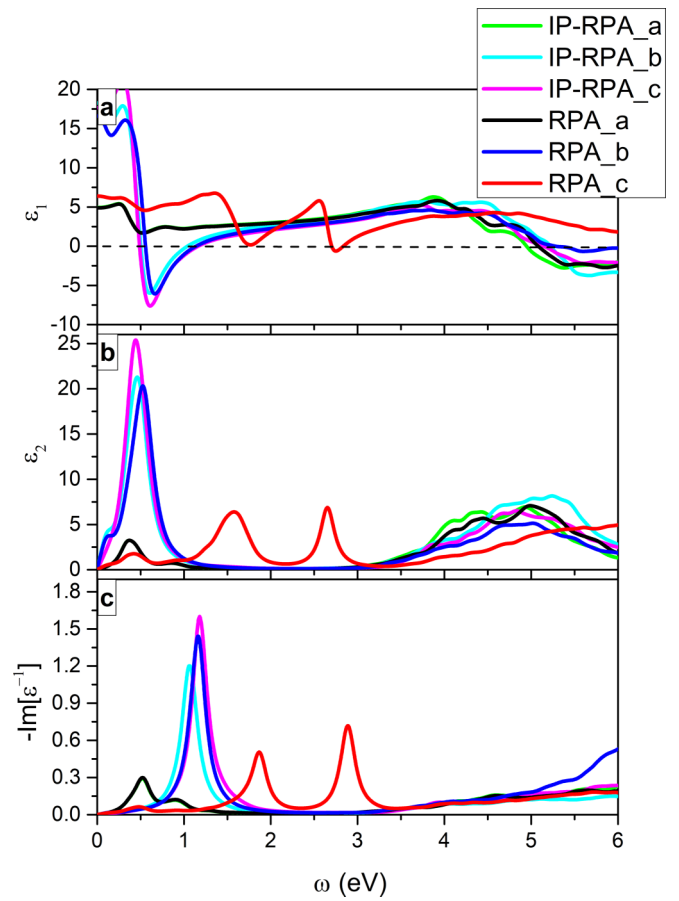

FIG. 8. Calculated macroscopic complex dielectric and loss functions of SrNbO$_{3.4}$ ($n = 5$) along the a, b, and c axes. (a) Real part, ε_1, and (b) imaginary part, ε_2, of the complex dielectric function and (c) loss function, $-\text{Im}[\varepsilon^{-1}]$. RPA and IP-RPA refer to the calculation with and without LFEs, respectively. The dashed horizontal line indicates the 0 of ε_1, to pinpoint the conventional plasmon peak energy.

pivotal role in creating multiple unconventional plasmons in the experiment.

Another influence of the EOP can be obtained by comparing results for SrNbO$_{3+\delta}$ with different oxygen contents. The structure of oxygen-rich SrNbO$_{3+\delta}$ compounds is strongly affected by the oxygen content and the thickness of each layer is given by the number of NbO$_6$ octahedra. As shown in Fig. 1, the thickness of each layer, which is separated by EOPs, can be tuned by varying the oxygen content. Without EOPs, an infinity member of Sr$_n$Nb$_n$O$_{3n+2}$ realizes SrNbO$_3$. Figure 9 shows the calculated RPA dielectric and loss functions of the layered strontium niobates with different oxygen contents. It is shown that the intensity and frequencies of unconventional plasmons are affected by the oxygen content, which further reflects the influence of the distance between two neighboring EOPs. Both the dielectric and the loss function can be altered by the thickness of slabs. The peaks of ε_2 and the loss function have negative correlations with the oxygen content. This is consistent with the fact that an increase in oxygen content reduces the free charge density. One could expect that a similar spectral shift can be achieved by introducing strain to reduce
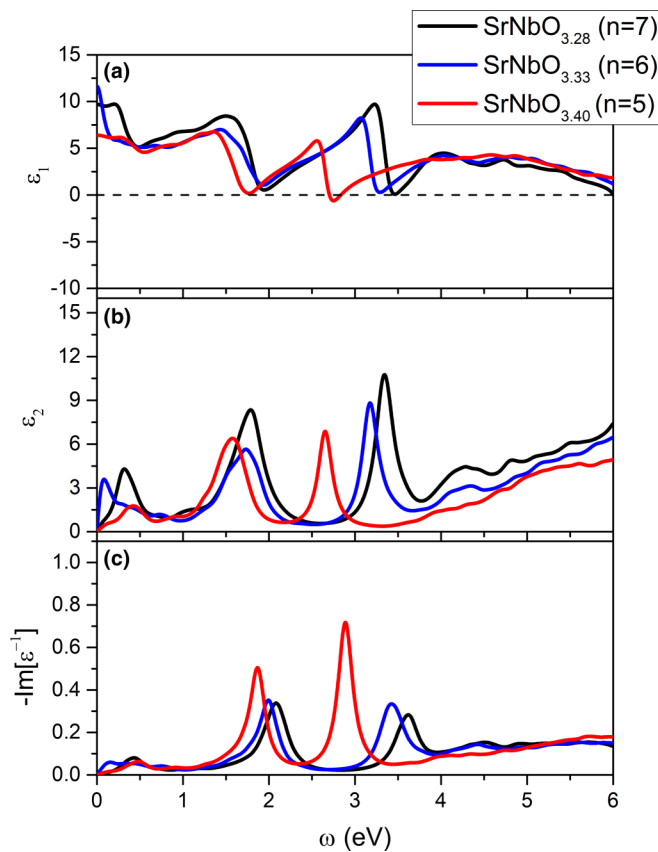
FIG. 9. Calculated macroscopic RPA dielectric and loss functions of SrNbO$_{3+\delta}$ with different oxygen contents. (a) Real part, ϵ_1, and (b) imaginary part, ϵ_2, of the complex dielectric function and (c) loss function, $-\text{Im}[\varepsilon^{-1}]$. The dashed horizontal line indicates the 0 of ε_1 to pinpoint the conventional plasmon peak energy.

or enlarge the distance between neighboring EOPs. The ε_1 of SrNbO$_{3.4}$ ($n = 5$) has negative values at plasmon energies $\sim$1.9 and $\sim$2.9 eV, which show a conventional character. However, the real dielectric function ε_1 of SrNbO$_{3.28}$ ($n = 7$) and SrNbO$_{3.33}$ ($n = 6$) [as well as SrNbO$_{3.4}$ ($n = 4, 6, \dots$)] remains positive from 0.6 to 6.0 eV. In this case, these plasmon

energies do not coincide with the 0 but instead coincide with the local minima of ε_1.

V. SUMMARY

We have analyzed the complex dielectric and loss functions of strontium niobate compounds of SrNbO$_3$ and SrNbO$_{3.4}$ and the alternating superstructure of SrNbO$_{3.3}$ and SrNbO$_{3.5}$. By performing fully *ab initio* calculations, we show that most of the unconventional plasmon behaviors in SrNbO$_{3.4}$ can be reproduced within the RPA when local field effects (LFEs) are considered. In the isotropic metallic SrNbO$_3$, a conventional plasmon is present and determined by both interband and intraband transitions. In insulatinglike SrNbO$_{3.4}$, the conventional plasmon is suppressed by LFEs, and through spectral weight transfer multiple frequencies and low-loss plasmons are generated. Consistent with experimental data, these plasmons are determined by an interplay of charge inhomogeneity induced by oxygen doping and the high polarizability induced by nonuniform growth of the sample. From our DFT analysis, we have inferred that these unconventional plasmons are collective excitations of electrons confined by the EOP. A strong anisotropy of the dielectric and loss functions is found. We further show that the frequencies of these plasmons can be tuned. Our result shows that this plasmon phenomenon with multiple resonances can be extended to other perovskite materials with strong electrical inhomogeneity.

[1] D. Ridgley and R. Ward, J. Am. Chem. Soc. **77**, 6132 (1955).

[2] K. Isawa, J. Sugiyama, K. Matsuura, A. Nozaki, and H. Yamauchi, Phys. Rev. B **47**, 2849 (1993).

[3] J.-E. Weber, C. Kegler, N. Büttgen, H.-A. Krug von Nidda, A. Loidl, and F. Lichtenberg, Phys. Rev. B **64**, 235414 (2001).

[4] A. Sakai, T. Kanno, K. Takahashi, Y. Yamada, and H. Adachi, J. Appl. Phys. **108**, 103706 (2010).

[5] W. Kobayashi, Y. Hayashi, M. Matsushita, Y. Yamamoto, I. Terasaki, A. Nakao, H. Nakao, Y. Murakami, Y. Moritomo, H. Yamauchi, and M. Karppinen, Phys. Rev. B **84**, 085118 (2011).

[6] F. Lichtenberg, A. Herrnberger, K. Wiedenmann, and J. Mannhart, Prog. Solid State Chem. **29**, 1 (2001).

[7] C. A. Kuntscher, S. Schuppler, P. Haas, B. Gorshunov, M. Dressel, M. Grioni, F. Lichtenberg, A. Herrnberger, F. Mayr, and J. Mannhart, Phys. Rev. Lett. **89**, 236403 (2002).

[8] C. A. Kuntscher, S. Schuppler, P. Haas, B. Gorshunov, M. Dressel, M. Grioni, and F. Lichtenberg, Phys. Rev. B **70**, 245123 (2004).

[9] C. Chen, S. Lv, Z. Wang, K. Akagi, F. Lichtenberg, Y. Ikuhara, and J. G. Bednorz, Appl. Phys. Lett. **105**, 221602 (2014).

[10] X. Xu, C. Randorn, P. Efstathiou, and J. T. S. Irvine, Nat. Mater. **11**, 595 (2012).

[11] D. Y. Wan, Y. L. Zhao, Y. Cai, T. C. Asmara, Z. Huang, J. Q. Chen, J. Hong, S. M. Yin, C. T. Nelson, M. R. Motapothula, B. X. Yan, D. Xiang, X. Chi, H. Zheng, W. Chen, R. Xu, Ariando, A. Rusydi, A. M. Minor, M. B. H. Breese, M. Sherburne, M. Asta, Q. H. Xu, and T. Venkatesan, Nat. Commun. **8**, 15070 (2017).

[12] T. C. Asmara, D. Y. Wan, Y. L. Zhao, M. A. Majidi, C. T. Nelson, M. C. Scott, Y. Cai, B. X. Yan, D. Schmidt, M. Yang,

T. Zhu, P. E. Trevisanutto, M. R. Motapothula, Y. P. Feng, M. B. H. Breese, M. Sherburne, M. Asta, A. Minor, T. Venkatesan, and A. Rusydi, Nat. Commun. **8**, 15271 (2017).

[13] A. Georges, G. Kotliar, W. Krauth, and M. J. Rozenberg, Rev. Mod. Phys. **68**, 13 (1996).

[14] G. Kotliar, S. Y. Savrasov, K. Haule, V. S. Oudovenko, O. Parcollet, and C. A. Marianetti, Rev. Mod. Phys. **78**, 865 (2006).

[15] E. G. C. P. van Loon, H. Hafermann, A. I. Lichtenstein, A. N. Rubtsov, and M. I. Katsnelson, Phys. Rev. Lett. **113**, 246407 (2014).

[16] S. L. Adler, Phys. Rev. **126**, 413 (1962).

[17] N. Wiser, Phys. Rev. **129**, 62 (1963).

[18] S. G. Louie, J. R. Chelikowsky, and M. L. Cohen, Phys. Rev. Lett. **34**, 155 (1975).

[19] K. Sturm, Phys. Rev. Lett. **40**, 1599 (1978).

[20] F. Aryasetiawan, O. Gunnarsson, M. Knupfer, and J. Fink, Phys. Rev. B **50**, 7311 (1994).

[21] S. Waidmann, M. Knupfer, B. Arnold, J. Fink, A. Fleszar, and W. Hanke, Phys. Rev. B **61**, 10149 (2000).

[22] P. Cudazzo, M. Gatti, and A. Rubio, New J. Phys. **15**, 125005 (2013).

[23] N. Vast, L. Reining, V. Olevano, P. Schattschneider, and B. Jouffrey, Phys. Rev. Lett. **88**, 037601 (2002).

[24] M. Gajdoš, K. Hummer, G. Kresse, J. Furthmüller, and F. Bechstedt, Phys. Rev. B **73**, 045112 (2006).

[25] H. Ehrenreich and M. H. Cohen, Phys. Rev. **115**, 786 (1959).

[26] G. Kresse and J. Furthmüller, Phys. Rev. B **54**, 11169 (1996).

[27] G. Kresse and D. Joubert, Phys. Rev. B **59**, 1758 (1999).

[28] P. E. Blöchl, Phys. Rev. B **50**, 17953 (1994).

[29] J. P. Perdew, K. Burke, and M. Ernzerhof, Phys. Rev. Lett. **77**, 3865 (1996).

[30] W. Kohn and L. Sham, Phys. Rev. **140**, A1133 (1965).

[31] H. J. Monkhorst and J. D. Pack, Phys. Rev. B **13**, 5188 (1976).

[32] G. Onida, L. Reining, and A. Rubio, Rev. Mod. Phys. **74**, 601 (2002).

[33] F. Sottile, F. Bruneval, A. G. Marinopoulos, L. K. Dash, S. Botti, V. Olevano, N. Vast, A. Rubio, and L, Reining, Int. J. Quantum Chem. **102**, 684 (2005).

[34] M. Cazzaniga, L. Caramella, N. Manini, and G. Onida, Phys. Rev. B **82**, 035104 (2010); www.dp-code.org.

[35] M. Gatti, F. Sottile, and L. Reining, Phys. Rev. B **91**, 195137 (2015).

[36] C. A. Kuntscher, S. Gerhold, N. Nücker, T. R. Cummins, D. H. Lu, S. Schuppler, C. S. Gopinath, F. Lichtenberg, J. Mannhart, and K. P. Bohnen, Phys. Rev. B **61**, 1876 (2000).